



**HAL**  
open science

# Characterization and Performance Analysis of a Chiral-Metamaterial Channel with Giant Optical Activity for Terahertz Communications

Anna Maria Vegni, Valeria Loscrì

► **To cite this version:**

Anna Maria Vegni, Valeria Loscrì. Characterization and Performance Analysis of a Chiral-Metamaterial Channel with Giant Optical Activity for Terahertz Communications. *Nano Communication Networks*, 2016, 9, pp.28-35. 10.1016/j.nancom.2016.07.004 . hal-01379904

**HAL Id: hal-01379904**

**<https://inria.hal.science/hal-01379904>**

Submitted on 14 Oct 2016

**HAL** is a multi-disciplinary open access archive for the deposit and dissemination of scientific research documents, whether they are published or not. The documents may come from teaching and research institutions in France or abroad, or from public or private research centers.

L'archive ouverte pluridisciplinaire **HAL**, est destinée au dépôt et à la diffusion de documents scientifiques de niveau recherche, publiés ou non, émanant des établissements d'enseignement et de recherche français ou étrangers, des laboratoires publics ou privés.

# Characterization and Performance Analysis of a Chiral-Metamaterial Channel with Giant Optical Activity for Terahertz Communications

Anna Maria Vegni<sup>a,\*</sup>, Valeria Loscri<sup>b</sup>

<sup>a</sup>*Department of Engineering, Roma Tre University, Rome, Italy*

<sup>b</sup>*INRIA Lille-Nord Europe, FUN Research Lab, Lille Nord-Europe, France.*

---

## Abstract

1 Technology in the THz frequency band has progressed rapidly in the last few  
2 years. The THz frequency band offers greater communication bandwidth than  
3 microwaves frequencies, and is becoming a standard for nanoscale communica-  
4 tions. Traditional channel models for lower frequencies do not take into consid-  
5 eration specific properties as the very high molecular absorption or the very high  
6 reflection loss. In addition, in a propagation medium exhibiting a Giant Optical  
7 Activity, it is also important to derive the characteristics of the channel affected by  
8 chirality effects. This phenomenon occurs in particular material known as chiral-  
9 metamaterials in the (4–10) THz band.

10 The main contribution of this paper consist in the analysis of specific parame-  
11 ters of a chiral-metamaterial, such as the relative electrical permittivity, magnetic  
12 permeability and chirality coefficients. These parameters are considered for the  
13 channel model derivation both in Line-of-Sight and No Line-of-Sight propagation.

14 The chiral effect affects the channel through the presence of spectral win-  
15 dows, due to peaks of resonance of chiral parameter. Performance analysis of the  
16 chirality-affected channel is assessed in terms of (i) channel capacity, (ii) propaga-

---

\*Corresponding author

17 tion delay, (iii) coherence bandwidth, and (iv) symbol rates, for different distances  
18 and propagation modes.

*Keywords:* THz band, chirality effects, Giant Optical Activity,  
nano-communications

---

## 1 **1. Introduction**

2 Over the last few years we have witnessed an increasing demand for much  
3 higher speed and ubiquitous wireless communication systems. Technological de-  
4 velopment pave the advent of new communication paradigms, such as the Internet  
5 of NanoThings [1]. Following this trend, the THz frequency band is rising as a  
6 very promising solution to enable ultra-high-speed communications with the aim  
7 to overcome the spectrum scarcity and capacity limitations of current wireless sys-  
8 tems. Advanced physical layer solutions are required, able to capture the specific  
9 and inherent features of the THz frequency bands. Indeed, traditional channel  
10 models for lower frequency bands cannot be adopted for THz communication.

11 Some new channel models have been presented for THz frequency bands [2,  
12 3, 4, 5, 6], where some of the specific characteristics of this frequency band, such  
13 as the high molecular absorption and the spreading loss, are taken into consider-  
14 ation and analyzed. Also, the analysis of signal propagation has been addressed  
15 in [7] through a multi-ray approach by assuming reflected, scattered and diffracted  
16 paths. As a result, the authors derived the main THz-band channel features, such  
17 as the distance-varying spectral windows, and the temporal broadening effects.

18 As it can be noticed from previous works, channel modeling in THz band  
19 is typically addressed through the study of its transfer functions that consider  
20 specific features, like molecular absorption loss or spreading loss, among oth-

1       ers. However, the previous models take into consideration some specific features  
2       of the channel at THz frequencies, but neglect other important effects that could  
3       play a very important role in the channel modeling. One of these properties is  
4       the electro-magnetic chirality effect and the specific features of the propagation  
5       medium. Chirality effect is the characteristic of some natural materials to ren-  
6       der an electric/magnetic response (displacement) under a magnetic/electric exci-  
7       tation (field), respectively. This effect can be recognized in the so-called natu-  
8       ral/artificial chiral materials. Examples of natural chiral materials are the sugar  
9       molecules (sucrose) or the cholesteric liquid crystals. Artificial chiral materials,  
10      *e.g.*, sculptured thin films [8], can be obtained by doping a natural dielectric with  
11      an amount of metallic/dielectric impurities each working as a couple of interacting  
12      electro-magnetic dipoles. These impurities generate the handedness experimen-  
13      tal evidence that prevents the superimposition of the molecular structure over a  
14      reverse copy of itself.

15       The relative chirality parameter is an intrinsic characteristic of a chiral homo-  
16      geneous isotropic medium. Standard values are in the range  $[0, 1]$ . We observe  
17      that in a specific range of the THz band, *i.e.*, (4-10) THz, the chiral parameter can  
18      reach very high values that vary with the frequency, and show a resonant behav-  
19      ior. Materials with this specific feature are said to exhibit a Giant Optical Activity  
20      (GOA). In particular media such as the chiral complex materials where a GOA  
21      takes place, the relative chirality parameter is complex and frequency-dependent,  
22      showing multiple peaks at specific resonance frequencies [9].

23       GOA material affected by chirality effects is generally called as *chiral-metamaterial* [10],  
24      due to the effect that the real part of relative electric permittivity and magnetic  
25      permeability of the material shows negative values, and are frequency-dependent.

1 This interesting property is of great interest to many areas of science, like analytical  
2 chemical chemistry and molecular biology. Finally, chiral-metamaterials are suitable  
3 media for the realization of nanosystem applications. Specifically, they represent  
4 the ideal candidates for operations in the THz band. In fact, in comparison to natural  
5 materials, chiral-metamaterials show a strong response to the THz radiation  
6 that represents a great technological potential in several sectors such as imaging,  
7 sensing, and also communications.

8 In this paper, we focus on GOA chiral-metamaterials, derive the channel transfer  
9 function and analyze its specific behavior in case of direct and multi-path propagation,  
10 in the (4–10) THz frequency range [9]. Due to the resonant behavior of  
11 chiral parameter, the channel model shows specific frequency-dependent spectral  
12 windows, guaranteeing high bandwidth values.

13 This paper is organized as follows. In Section 2 we introduce the frequency-  
14 dependent behavior of specific parameters of a chiral-metamaterial. Starting from  
15 the concept of electro-magnetic chirality [11, 12, 13], we consider the chiral effects  
16 following the change in the propagation velocity and in the refractive index,  
17 due to the chiral impurities inside the propagation medium. These effects are evaluated  
18 also in the case when the considered medium exhibits a GOA [9, 14]. Then,  
19 in Section 3 we derive the corresponding chirality-affected channel model for THz  
20 band, and present the related frequency-dependent spectral windows. Section 4 is  
21 then devoted to the performances of the chiral channel, assessed in terms of capacity,  
22 propagation delay, coherence bandwidth, and symbol rates, in case of LoS  
23 and NLoS propagation modes. Finally, conclusions are drawn at the end of the  
24 paper.

## 1      2. Full-Wave Propagation Model in a Chiral-Metamaterial

2            Starting from the classic harmonic macroscopic Maxwell's equations, we con-  
3            sider the electro-magnetic propagation inside a generic complex material, under  
4            the assumption that it is a linear and chiral medium.

5            Unconventional materials (*i.e.*, metamaterials) are specifically considered since  
6            the GOA is reinforced by using thin metallic crossed-structure impurities in the  
7            host dielectric medium, that is chiral-metamaterials [10]. Therefore, we consider  
8            a time-harmonic generic linear material, where chiral (magneto/electric-optical)  
9            effects are included in the following constitutive relations, written as:

$$10 \quad \left\{ \begin{array}{l} \mathbf{B} = \underline{\xi} \bullet \mathbf{E} + \underline{\mu} \bullet \mathbf{H} \\ \mathbf{D} = \underline{\varepsilon} \bullet \mathbf{E} + \underline{\zeta} \bullet \mathbf{H} \end{array} \right. \quad (1)$$

11            where we remind that  $\mathbf{B}$  is the magnetic displacement and  $\mathbf{H}$  is the magnetic field,  
12            as well as  $\mathbf{D}$  is the electric displacement and  $\mathbf{E}$  is the electric field. Finally, the  
13            symbol  $\bullet$  represents the scalar product operator, and  $\underline{\xi}$ ,  $\underline{\mu}$ ,  $\underline{\varepsilon}$ , and  $\underline{\zeta}$  are specific  
14            tensor quantities of the material.

15            From (1) we observe the chirality property through the dependence of (i)  $\mathbf{E}$   
16            in  $\mathbf{B}$ , and (ii)  $\mathbf{H}$  in  $\mathbf{D}$ . Furthermore, the displacement field existing inside the  
17            material is generated by an excitation expressed in terms of intensity of the inci-  
18            dent electro-magnetic field. Therefore, the material under consideration is a linear  
19            chiral medium.

20            We remind that the chiral effects have a two-fold meaning, *i.e.*, (i) an electric  
21            field applied on the material provides not only an electric induction, but also a  
22            magnetic displacement, and (ii) a magnetic field applied on the material provides  
23            not only a magnetic induction, but also an electric displacement, unlike from non-

1 chiral materials.

2 As previously said, in this paper our attention is devoted to GOA chiral-  
 3 metamaterials [15], where the authors show that for a GOA reciprocal material  
 4 the specific constitutive relations are as follows:

$$5 \quad \begin{bmatrix} \mathbf{B} \\ \mathbf{D} \end{bmatrix} = \begin{bmatrix} -j\frac{\xi_0\xi_r}{c} & \mu_0\mu_r \\ \varepsilon_0\varepsilon_r & j\frac{\xi_0\xi_r}{c} \end{bmatrix} \bullet \begin{bmatrix} \mathbf{E} \\ \mathbf{H} \end{bmatrix}, \quad (2)$$

6 where it is clear that the natural dielectric (where  $\varepsilon_b$  and  $\mu_b$  are the permittivity and  
 7 permeability, respectively) becomes a metamaterial. Moreover, according to [15],  
 8 at the frequency around 5 THz and 8 THz, there are four resonance frequencies of  
 9 the  $\xi_r$  relative chirality parameter, *i.e.*, [4.8, 5.6, 7.9, 8.2] THz.

10 The same consideration is applied to the relative permittivity and permeability  
 11 parameters, still in the (4–10) THz band. As reported in [9, 16],  $\varepsilon_r$  and  $\mu_r$  are  
 12 complex parameters, and the real part has a frequency-dependent behavior with  
 13 resonant peaks.

14 Equation (2) becomes

$$15 \quad \begin{bmatrix} \mathbf{B} \\ \mathbf{D} \end{bmatrix} = \begin{bmatrix} -j\frac{\Omega_\xi\omega_0\omega}{\omega_0^2-\omega^2-j\omega\gamma} & \mu_0\left(\mu_b + \frac{\Omega_\mu\omega^2}{\omega_0^2-\omega^2-j\omega\gamma}\right) \\ \varepsilon_0\left(\varepsilon_b + \frac{\Omega_\varepsilon\omega_0^2}{\omega_0^2-\omega^2-j\omega\gamma}\right) & j\frac{\Omega_\xi\omega_0\omega}{\omega_0^2-\omega^2-j\omega\gamma} \end{bmatrix} \bullet \begin{bmatrix} \mathbf{E} \\ \mathbf{H} \end{bmatrix}, \quad (3)$$

16 where  $\omega = 2\pi f$ ,  $\varepsilon_0$ , and  $\mu_0$  are the absolute permittivity and permeability, respec-

1 tively. Then, the constitutive parameters of interest are:

$$2 \quad \varepsilon = \varepsilon_0 \varepsilon_r = \varepsilon_0 \left[ \varepsilon_b + \Omega_\varepsilon \omega_0^2 \left( \frac{\omega_0^2 - \omega^2 + j\omega\gamma}{(\omega_0^2 - \omega^2)^2 + \omega^2 \gamma^2} \right) \right], \quad (4)$$

$$3 \quad \mu = \mu_0 \mu_r = \mu_0 \left[ \mu_b + \Omega_\mu \omega^2 \left( \frac{\omega_0^2 - \omega^2 + j\omega\gamma}{(\omega_0^2 - \omega^2)^2 + \omega^2 \gamma^2} \right) \right], \quad (5)$$

$$4 \quad \xi_r = \Omega_\xi \omega_0 \omega \left( \frac{\omega_0^2 - \omega^2 + j\omega\gamma}{(\omega_0^2 - \omega^2)^2 + \omega^2 \gamma^2} \right). \quad (6)$$

7 It is noted that the frequency resonant behavior of  $\xi_r$  is a Drude-like one, and  $\Omega_\varepsilon$ ,  
8  $\Omega_\mu$ ,  $\Omega_\xi$ ,  $\gamma$ , and  $\omega_0$  are specific parameters of the GOA material [15].

9 By simple computations, and assuming a lossy material, *i.e.*,

$$10 \quad \begin{cases} \varepsilon_b = \text{Re} [\varepsilon_b] + j \text{Im} [\varepsilon_b] \\ \mu_b = \text{Re} [\mu_b] + j \text{Im} [\mu_b] \end{cases} \quad (7)$$

11 we obtain

$$12 \quad \varepsilon_r = \left( \text{Re} [\varepsilon_b] + \frac{\omega_0^2 (\omega_0^2 - \omega^2) \Omega_\varepsilon}{(\omega_0^2 - \omega^2)^2 + \omega^2 \gamma^2} \right) + \quad (8)$$

$$13 \quad j \left( \frac{\gamma \omega_0^2 \Omega_\varepsilon \omega}{(\omega_0^2 - \omega^2)^2 + \omega^2 \gamma^2} + \text{Im} [\varepsilon_b] \right),$$

$$14 \quad \mu_r = \left( \text{Re} [\mu_b] + \frac{\omega^2 (\omega_0^2 - \omega^2) \Omega_\mu}{(\omega_0^2 - \omega^2)^2 + \omega^2 \gamma^2} \right) + \quad (9)$$

$$15 \quad j \left( \frac{\gamma \Omega_\mu \omega^3}{(\omega_0^2 - \omega^2)^2 + \omega^2 \gamma^2} + \text{Im} [\mu_b] \right),$$

$$16 \quad \xi_r = \omega_0 \Omega_\xi \left[ \frac{\omega (\omega_0^2 - \omega^2)}{(\omega_0^2 - \omega^2)^2 + \omega^2 \gamma^2} \right] + j \omega_0 \Omega_\xi \left[ \frac{\gamma \omega^2}{(\omega_0^2 - \omega^2)^2 + \omega^2 \gamma^2} \right]. \quad (10)$$

17 Now, by posing the following expression for the square relative refractive in-



1 dex:

$$2 \quad \varepsilon_r \mu_r + \xi_r^2 = (\text{Re} [\varepsilon_r] + j\text{Im} [\varepsilon_r]) (\text{Re} [\mu_r] + j\text{Im} [\mu_r]) + \quad (11)$$

$$3 \quad + (\text{Re} [\xi_r] + j\text{Im} [\xi_r])^2 > 0,$$

3 we observe that the following conditions hold for a GOA material:

$$4 \quad \Omega_\varepsilon = \left( 1 + \frac{\gamma^2}{\omega^2 - \omega_0^2} \right) \text{Re} [\varepsilon_b], \quad (12)$$

$$5 \quad \Omega_\mu = \left( 1 + \frac{\gamma^2}{\omega^2 - \omega_0^2} \right) \text{Re} [\mu_b], \quad (13)$$

$$6 \quad \Omega_\xi = \left( 1 + \frac{\gamma^2}{\omega^2 - \omega_0^2} \right) \sqrt{\text{Re} [\varepsilon_b] \text{Re} [\mu_b]}. \quad (14)$$

7 It is observed that relations (12), (13), and (14) state the connection between the  
 8 host material parameters, *i.e.*,  $\varepsilon_b$ , and  $\mu_b$ , and the specific GOA ones in order to  
 9 obtain a positive refractive index in (11).

10 Finally, the computation of the electro-magnetic field in the channel is carried  
 11 out through the solutions of linear differential equations, arising from the follow-  
 12 ing source-less Maxwell's equations:

$$13 \quad \begin{cases} (\nabla + j\omega\underline{\xi}) \bullet \mathbf{E} = -j\omega\underline{\mu} \bullet \mathbf{H} \\ (\nabla - j\omega\underline{\zeta}) \bullet \mathbf{H} = j\omega\underline{\varepsilon} \bullet \mathbf{E} \end{cases} \quad (15)$$

14 and the solving differential equations for  $\mathbf{E}$  and  $\mathbf{H}$  are given, respectively:

$$15 \quad \begin{cases} [(\nabla - j\omega\underline{\zeta}) \bullet \underline{\mu}^{-1} \bullet (\nabla + j\omega\underline{\xi}) - \omega^2\underline{\varepsilon}] \bullet \mathbf{E} = 0 \\ [(\nabla + j\omega\underline{\xi}) \bullet \underline{\varepsilon}^{-1} \bullet (\nabla - j\omega\underline{\zeta}) - \omega^2\underline{\mu}] \bullet \mathbf{H} = 0 \end{cases} \quad (16)$$

16 where  $\nabla$  is Kong's operator.

1 As a noteworthy point, we can examine how the constitutive relations influ-  
 2 ence the channel polarization properties. Typically, the antenna at the transmitter  
 3 side is a radiating element that can be linearly or circularly polarized. In these  
 4 two cases we obtain interesting features of the channel directly connected with  
 5 the constitutive relations of the medium. Namely, by assuming the linear polar-  
 6 ization of the electric field generated by an appropriate antenna (*i.e.*,  $\mathbf{E} = E_x \hat{\mathbf{x}}$ ),  
 7 we obtain the final second order partial differential equation for  $E_x$ , *i.e.*,

$$8 \quad \alpha_1 E_x + \alpha_2 \frac{\partial E_x}{\partial x} + \alpha_3 \frac{\partial E_x}{\partial y} + \alpha_4 \frac{\partial E_x}{\partial z} + \alpha_5 \frac{\partial^2 E_x}{\partial y^2} + \alpha_6 \frac{\partial^2 E_x}{\partial z^2} = 0, \quad (17)$$

9 where  $\alpha_i$  with  $i = (1, 2, \dots, 6)$  are coefficients depending on the elements of  $\underline{\varepsilon}$ ,  $\underline{\mu}$ ,  
 10  $\underline{\xi}$ , and  $\underline{\zeta}$  tensors.

11 On the other side, for a circularly polarized antenna, *i.e.*,  $\mathbf{E} = E_x \hat{\mathbf{x}} + E_y \hat{\mathbf{y}} =$   
 12  $E_x \hat{\mathbf{x}} + j(\pm) E_x \hat{\mathbf{y}}$ , the final second order partial differential equation for  $E_x$  is  
 13 obtained:

$$14 \quad \gamma_1 E_x + \gamma_2 \frac{\partial^2 E_x}{\partial x^2} + \gamma_3 \frac{\partial^2 E_x}{\partial x \partial y} + \gamma_4 \frac{\partial^2 E_x}{\partial x \partial z} + \gamma_5 \frac{\partial^2 E_x}{\partial y^2} + \gamma_6 \frac{\partial^2 E_x}{\partial y \partial z} + \gamma_7 \frac{\partial^2 E_x}{\partial z^2} = 0, \quad (18)$$

15 where  $\gamma_j$  with  $j = (1, 2, \dots, 7)$  are coefficients depending on the elements of  $\underline{\varepsilon}$ ,  
 16  $\underline{\mu}$ ,  $\underline{\xi}$ , and  $\underline{\zeta}$  tensors. Equations (17) and (18) allow to classify the transmission  
 17 properties of the channel according to the choice of the transmitting medium.  
 18 Therefore, such formulas are useful as design tools for materials working in THz  
 19 band, including GOA materials and optical metamaterials.

20 Notice that  $\alpha_i$  and  $\gamma_j$  parameters can be described through 36 degrees of free-  
 21 dom as a consequence of their dependance on  $\underline{\varepsilon}$ ,  $\underline{\mu}$ ,  $\underline{\xi}$ , and  $\underline{\zeta}$  tensors. This means  
 22 that we have a lot of partial differential linear equations similar to (17) and (18)

1 that should be examined in order to determine the corresponding propagation char-  
 2 acteristics of the channel. However, as future work, we can investigate this point  
 3 by starting from a topology of channel material (*e.g.*, bianisotropic, biaxial, etc.)  
 4 and then determine the specific transmission/ reflection related properties.

### 5 **3. Chiral-affected Channel Model**

6 In this section, we present how the relative chirality parameter affects the  
 7 channel performance in the (4–10) THz band, in the case of ray tracing propaga-  
 8 tion (*i.e.*, LoS, and NLoS), and under the linear polarization hypothesis. Specifi-  
 9 cally, in NLoS case, we focus on reflected paths due at generic reflection centers  
 10 located at  $z$ -plane. The reflection characteristics of the transmissive channel can  
 11 be evaluated through the specific knowledge of the local planar geometry associ-  
 12 ated to the reflection centers.

13 The use of ray tracing techniques for channel modeling in THz band has been  
 14 largely adopted, like in [5], where Han *et al.* consider a multi-ray approach with  
 15 one direct path, and other reflected, scattered, and diffracted paths. According to  
 16 this approach, the channel model is the combination of several individual narrow  
 17 sub-bands, each of them with a flat-band response. Assuming  $N_i$  narrow sub-  
 18 bands, and in the case of stationary environment, the channel response in the  $i$ -th  
 19 sub-band is given as

$$20 \quad h_i(\tau) = \sum_{n=1}^{N_i} \alpha_{i,n} \delta(\tau - \tau_n), \quad (19)$$

21 where  $\alpha_{i,n}$  is the frequency-dependent attenuation, and  $\tau_n$  is the propagation delay  
 22 of the  $n$ -th ray in the multi-ray approach.

23 From (19), and according to the computations in [5], we can derive the LoS

1 and NLoS channel transfer functions in the case of chirality-affected channel with  
 2 GOA, respectively as:

$$3 \quad H_{\text{LoS}}(f) = H_{\text{Abs}}(f) H_{\text{Spr}}(f) e^{-j2\pi f \tau_{\text{LoS}}}, \quad (20)$$

4 and

$$5 \quad H_{\text{NLoS}}(f) = \left[ \frac{\nu_c}{4\pi f (d_1 + d_2)} \right] e^{-j2\pi f \tau_{\text{NLoS}} - \frac{1}{2}k(f)(d_1 + d_2)} \cdot R(f), \quad (21)$$

6 where we assume the NLoS scenario is affected by reflected rays only, through  
 7 the rough surface reflection loss, *i.e.*,  $R(f)$ .

8 In (20),  $H_{\text{Abs}}$  is the transfer function due to the molecular absorption loss,  
 9 while  $H_{\text{Spr}}$  is the spreading loss that takes account for the chirality effect through  
 10  $\nu_c$  that is the propagation velocity of the electro-magnetic field in a chiral homo-  
 11 geneous isotropic medium, *i.e.*,

$$12 \quad \nu_c = \frac{c}{n_c}, \quad (22)$$

13 where  $c$  is the light propagation speed, and  $n_c$  is the refractive index in a chiral  
 14 medium, *i.e.*,

$$15 \quad n_c = \sqrt{\mu_r \varepsilon_r + \xi_r^2}, \quad (23)$$

16 with  $\mu_r$ ,  $\varepsilon_r$  and  $\xi_r$  frequency-dependent parameters, as depicted in [16]. Finally,  
 17 under the hypothesis of stationary scenario where the transmitter and the receiver  
 18 are at a distance  $d$  [m], from (20) we obtain the propagation delay for the LoS ray  
 19 as:

$$20 \quad \tau_{\text{LoS}} = \frac{d}{\nu_c}. \quad (24)$$

21 For the NLoS channel transfer function expressed in (21), by assuming  $d_1$  as

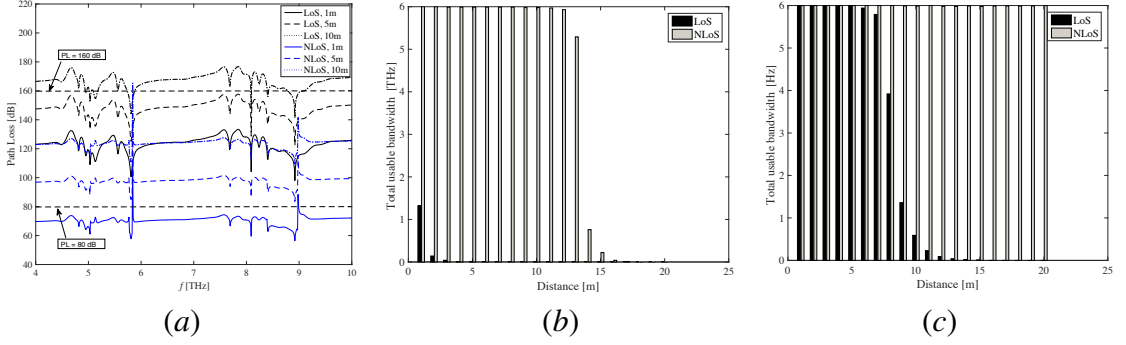


Figure 1: Spectral windows in a chiral-affected channel with GOA. (a) Path loss, and (b) total usage bandwidth for LoS and NLoS propagation in case of a path loss threshold of 120 dB, and (c) 160 dB.

1 the distance between the transmitter and a generic reflecting point, and  $d_2$  as the  
 2 distance between this point and the receiver, we obtain the propagation delay of  
 3 the  $j$ -th NLoS ray along the distance  $(d_1 + d_2)$ , as

$$4 \quad \tau_{\text{NLoS}} = \frac{d_1 + d_2}{\nu_c}. \quad (25)$$

5 From the expressions of channel transfer functions in (20) and (21), it is easy  
 6 to compute the total path loss, as depicted in Figure 1 (a) in case of LoS and NLoS  
 7 propagations, for different distances from transmitter to receiver, and assuming a  
 8 specific reflecting angle for multi-path. The expressions of path loss in LoS and  
 9 NLoS are respectively:

$$10 \quad A_{\text{LoS}} = A_s + A_a = 20 \log_{10} \left( \frac{4\pi d}{\lambda_{\text{Chir}}} \right) + 10\gamma d \log_{10} e, \quad (26)$$

1 and

$$\begin{aligned}
 2 \quad A_{\text{NLoS}} &= 10\log_{10} \left( \frac{\nu_c}{4\pi f(d_1+d_2)} \right) + \\
 &+ 10\log_{10} \left( e^{-\frac{1}{2}\alpha(d_1+d_2)} e^{-\frac{2\cos(\beta_i)}{\sqrt{n_c^2-1}}} e^{-\frac{8\pi^2 f^2 \sigma^2 \cos^2(\beta_i)}{\nu_c^2}} \right). \quad (27)
 \end{aligned}$$

3 where  $\lambda_c = \nu_c/f$  is the wavelength in the considered medium affected by the  
 4 homogeneous chirality, and  $\gamma$  is the absorption coefficient measuring the amount  
 5 of absorption loss of the EM field in the medium.

6 From Figure 1, by increasing the distance, the path loss has a higher trend.  
 7 Moreover, similarly to the results in [7], the LoS propagation (black lines) pro-  
 8 vides higher values with respect to the NLoS scenario (blue lines). In both LoS  
 9 and NLoS, the behavior is frequency-dependent, but in LoS propagation the path  
 10 loss has a smoother trend, with some peaks at 5.8, 8.09 and 8.93 THz. On the other  
 11 hand, for NLoS propagation, the peaks are well noticeable at 5.8 and 8.93 THz,  
 12 while on the other frequencies, the trend is on average flat around 70, 100 and  
 13 120 dB for LoS at  $d = 1, 5, \text{ and } 10$  m, respectively.

14 Similarly to the analysis conducted in [7], we aim to characterize the spectral  
 15 windows of chiral channel transfer functions in case of LoS and NLoS propaga-  
 16 tion. A spectral window is given by the portion of spectrum below a given path  
 17 loss threshold. We expect to observe that the path loss peaks caused by the chiral  
 18 effect create several spectral windows, with different bandwidths in each of them.

19 In the case of a path loss threshold set to 80 dB, the communication distance is  
 20 limited for NLoS propagation at lower distance of 1 m, except the two peaks that  
 21 are above this threshold, and correspond to 5.84 THz and 8.98 THz. According  
 22 to the values assumed in [7], the threshold of 80 dB corresponds to no gains of  
 23 transmission and reception antennas, and so to a multi-path propagation model.

1           In order to identify the spectral windows for LoS propagation, we have to in-  
2           crease the path loss threshold around 120 dB, so that a few windows appear for  
3           a distance of 1 m (see curve LoS for  $d = 1$  m in Figure 1 (a)). However, in  
4           this case most of the path loss for LoS propagation is above the threshold, thus  
5           providing a reduced usable bandwidth. Figure 1 (b) depicts the usable bandwidth  
6           versus the distance for the path loss threshold of 120 dB. We notice that the avail-  
7           able spectrum in LoS propagation is limited up to 4 m, reaching a maximum at  
8           1.32 THz corresponding to a distance of 1 m. In contrast, the NLoS propagation  
9           reaches higher bandwidths, and then it decreases at 17 m where the bandwidth is  
10          0.01 THz. The bandwidth rate in LoS is 75.5 GHz/m, while it reaches 3.90 THz/m  
11          in NLoS scenario.

12          It follows that an increase of the path loss threshold to 160 dB is expected  
13          to provide higher values of usable bandwidth in LoS propagation, as depicted in  
14          Figure 1 (c). Higher path loss thresholds rise from higher antenna gains, and the  
15          transmission becomes directional through the LoS path. In this case, the usable  
16          bandwidth in LoS propagation reaches higher values than those for the threshold  
17          of 120 dB. The lowest value is 0.01 THz for a distance of 15 m, and the average  
18          bandwidth rate for LoS propagation is 2.39 THz/m.

19          On the other side, for NLoS propagation, the usable bandwidth reaches ap-  
20          proximately the maximum value of 6 THz for different distances, and then the  
21          average rate of the total usable bandwidth is 5.99 THz/m. As a result, we can  
22          conclude that within the range (4–10) THz the available bandwidth is almost the  
23          entire band, especially for NLoS propagation.

24          Notice that in this paper, we focus only on the transfer functions in LoS and  
25          NLoS scenarios in a chirality-affected channel, assuming a flat behavior for the

1 molecular absorption loss (frequency independent behavior). Then, in all the  
 2 simulation results we omit the frequency-dependent molecular absorption effect.  
 3 Specifically, in NLoS we assume the presence of reflected rays only, since we are  
 4 interested in the behavior of highly frequency-dependent reflections that depend  
 5 on the shape, material, and roughness of the reflecting surface affects the THz  
 6 wave propagation.

#### 7 **4. Chiral Channel Characterization**

8 Following the chirality-affected channel model presented in Section 3, in this  
 9 section we investigate its main features in the (4–10) THz band. Specifically, we  
 10 aim to characterize (i) the channel capacity, (ii) the propagation delay, (iii) the  
 11 coherence bandwidth, and (iv) the symbol rate.

##### 12 *4.1. Channel capacity and propagation delay*

13 To evaluate the capacity limits in a chiral medium, we refer to the approach  
 14 adopted in [5], where the received signal has been decomposed as a sum of the  
 15 sub-bands, each one with a narrow behavior and a flat-band response. The follow-  
 16 ing constraint is adopted:

$$17 \quad \sum_{i=1}^{N_B} P_i \leq P_{TOT}, \quad (28)$$

18 where  $N_B$  is the total number of sub-bands,  $P_i$  is the transmission power in the  $i$ -  
 19 th sub-band, and  $P_{TOT}$  is the total transmit power in the (4–10) THz band. Notice  
 20 that, since the chiral parameter has a frequency-dependent behavior in (4–10) THz  
 21 band, we consider only this frequency range.

1 For  $N_B$  sub-bands, the capacity can be defined as the sum of the single capac-



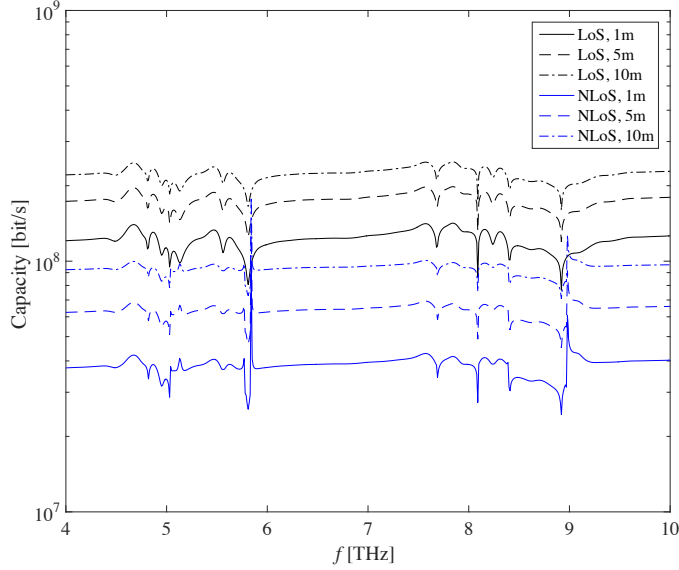


Figure 2: Capacity per sub-band of a chirality-affected channel with GOA, versus frequency for LoS and NLoS propagation, and different distances.

ities in each sub-band, *i.e.*,

$$C = \sum_{i=1}^{N_B} C_i = \sum_{i=1}^{N_B} \Delta f_i \log \left( 1 + \frac{|h_i|^2 P_i}{\Delta f_i S_N(f_i)} \right), \quad (29)$$

where  $S_N$  is the power spectral density of the additive white Gaussian noise, and  $\Delta f_i$  is the sub-band range among two consecutive sub-bands, *i.e.*,  $\Delta f_i = f_{i+1} - f_i$ , assumed as 10 GHz in our simulation results. We assume a flat power profile, that is the total power transmission is uniformly distributed over the entire operative band (*i.e.*, from 4 to 10 THz). Also, we consider a power level of 46 dBm, divided across all the sub-bands, *i.e.*,  $N_B = 600$ .

Figure 2 depicts the chirality-affected channel capacity with GOA in case of LoS and NLoS scenario. We notice that with a reduction of distance, the capacity decreases as well, and also the LoS scenario has a smoother behavior with respect

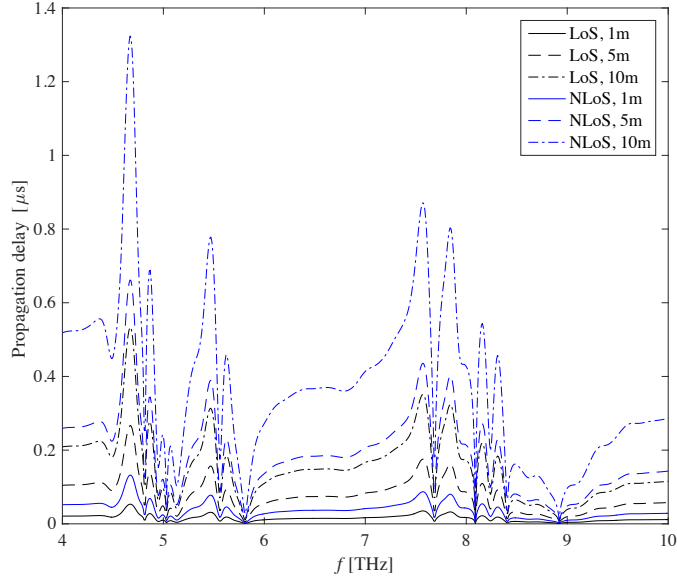


Figure 3: Propagation delay versus frequency in a chirality-affected channel with GOA, for LoS and NLoS propagation, and different distances.

2 to the frequency, while the NLoS shows an accentuate frequency-dependent trend,  
3 with distinguishable peaks at resonance frequencies. Specifically, in LoS, the  
4 capacity has an almost flat behavior, with a mean value of 0.22 Gbit/s for  $d =$   
5 10 m. Performances get worst in the case of NLoS propagation for  $d = 1$  m,  
6 where we observe a degradation of capacity at 5.81 and 8.92 THz, corresponding  
7 to 25.65 Mbit/s and 24.47 Mbit/s, respectively.

8 From the expressions in (24) and (25), the propagation delay in LoS and NLoS  
9 scenarios is depicted in Figure 3. We observe the frequency-dependent behavior  
10 due to the chiral effect, and as expected, performance gets worst when the distance  
11 increases. An almost-flat behavior is shown for LoS at short distances (*i.e.*,  $d =$   
12 1 m), while a resonant trend appears when increasing the distance, as well as in  
13 NLoS scenario due to the longer distances covered. Finally, we observe that the  
1 propagation delay both in LoS and NLoS case shows lower values corresponding

2 to 5.81 and 8.92 THz.

### 3 4.2. Coherence bandwidth and symbol rate

4 The root mean square (rms) delay spread is a measure of how dispersive the  
5 channel is. It is expressed as [7]:

$$6 \quad \sigma_i = \sqrt{\overline{\tau_i^2} - \overline{\tau_i}^2}, \quad (30)$$

7 where  $\overline{\tau_i}$  and  $\overline{\tau_i^2}$  are the first and second moments of the instantaneous power-delay  
8 profile, respectively. From (30) we can derive information about the coherence  
9 bandwidth, defined as the range of frequencies over which the channel correlation  
10 exceeds 50%.

11 In our simulations, we consider two scenarios with a variable number of NLoS  
12 reflected rays, *i.e.*, (i) one, and (ii) five, and one direct ray. In both cases, we  
13 observe the frequency-dependent behavior as typical of chiral materials exhibiting  
14 GOA. In Figure 4 (a) we show the coherence bandwidth in the case of one LoS  
15 and one NLoS path for different distances. As experienced in [5], higher values  
16 are reached for shorter distances. However, we cannot compare our results to  
17 others obtained with pre-existing approaches, since the frequency range is not the  
18 same.

19 In our simulations, several peaks appear due to the chirality effects. This can  
20 allow tuning the frequency to resonant peaks in order to obtain higher perfor-  
21 mances. For example, for  $d = 1$  m, the minimum value of rms delay is 0.33 ns,  
22 corresponding to 8.92 THz. This value corresponds to a symbol rate limited to  
23  $0.1/\sigma_i = 0.29$  Gbit/s to avoid inter-symbol interference. Also, in this case, the  
1 coherence bandwidth is limited to 0.59 GHz at the frequency peak of 8.92 THz.

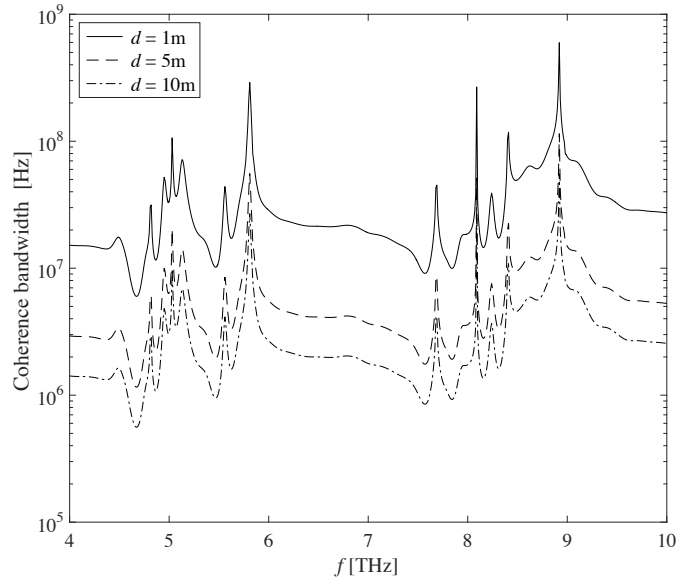
2 On the other side, when the distance increases (*i.e.*,  $d = 10$  m), the minimum  
3 rms delay is 3.6 ns at 8.92 THz. This value provides a symbol rate limited to  
4 27.71 Mbit/s, and the coherence bandwidth equals to 55.43 MHz, still at the same  
5 frequency.

6 Performances get worst in case of multiple reflected paths, as shown in Fig-  
7 ure 4 (b). For  $d = 1$  m the minimum rms is 0.78 ns, which corresponds to a  
8 coherence bandwidth of 0.25 GHz. For higher distances (*i.e.*,  $d = 10$  m) the  
9 minimum rms is 7.31 ns, corresponding to a coherence bandwidth is 27.3 MHz.

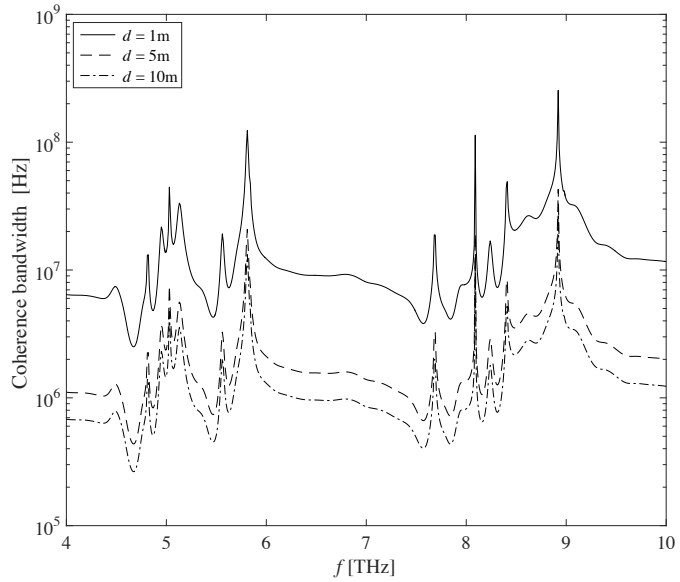
10 Finally, following the analysis of coherence bandwidths, we can derive the  
11 symbol rates in different scenarios, as depicted in Figure 5 (a) and (b) in case of  
12 (a) one LoS and one NLoS path, and (b) one LoS and five reflected NLoS paths,  
13 respectively. We notice the symbol rate is limited to a maximum of 0.29 Gbit/s  
14 corresponding to 8.92 THz, in order to avoid InterSymbol Interference (ISI) for  
15 linearly-modulated signals. Again, the chiral frequency behavior is observed, and  
16 a decrease of symbol rate is experienced for increasing distances (*e.g.*, for  $d =$   
17 10 m the symbol rate reaches 0.27 Mbit/s at 4.67 THz). Finally, as depicted in  
18 Figure 5 (b) an increase of reflected NLoS paths affects the symbol rate, then  
19 causing a decrease of performances until 0.13 Mbit/s for  $d = 10$  m at 4.67 THz,  
20 while the maximum value is 0.12 Gbit/s obtained for  $d = 1$  m at the frequency of  
21 8.92 THz.

## 22 5. Conclusions

23 In this paper we have derived the channel transfer function of a GOA chirality  
24 affected channel, both in the case of LoS and NLoS propagation in the (4–10) THz  
1 band.

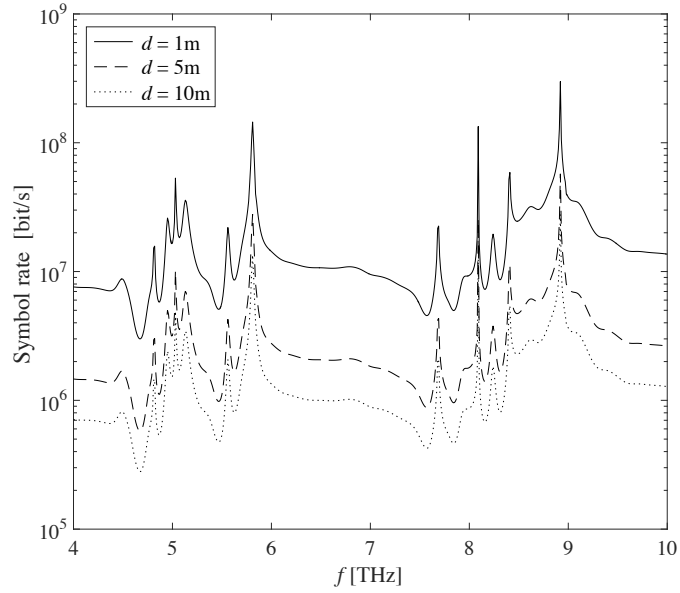


(a)

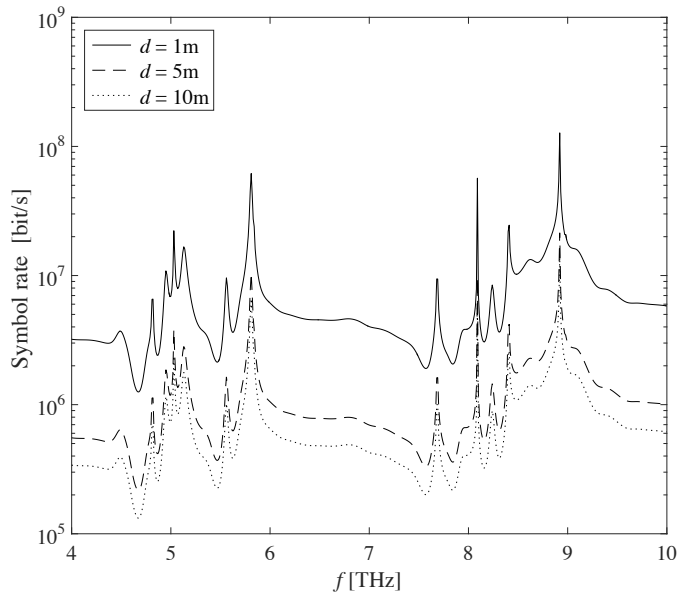


(b)

Figure 4: Coherence bandwidth in a chirality-affected channel with GOA, in case of (a) one LoS and one NLoS path, an (b) one LoS and five NLoS paths.



(a)



(b)

Figure 5: Symbol rates versus frequency in a chirality-affected channel with GOA, for different distances from transmitter to receiver, in case of (a) one LoS and one NLoS path, an (b) one LoS and five NLoS paths.

2        We considered the effects of the relative chiral parameter, assuming a frequency-  
3 dependent behavior with resonant peaks at specific frequencies. As a result, this  
4 affects the channel transfer function, as well as other performances. In particular,  
5 we identified the spectral windows that rise from the chiral effect, and the asso-  
6 ciated usable bandwidths. The spectral windows vary with the distance and the  
7 frequency, with corresponding bandwidths up to 6 THz, both in LoS and NLoS  
8 propagation. Another contribution of the paper has been in the identification of  
9 specific frequencies that allow high performance to be achieved. Thanks to the  
10 frequency-dependent behavior of a chiral-metamaterial, we can tune the working  
11 frequency in order to maximize the performance. Just as an example, the rms  
12 delay is dependent on the distance and carrier frequency, and reaches minimum  
13 values at 8.92 THz, corresponding to higher coherence bandwidths.

14        As conclusion of this paper, we can claim that GOA metamaterial present-  
15 ing chirality effects, are really promising in terms of performance that can be  
16 achieved, above all in the case of lower distances. Also, distance-adaptive and  
17 multi-carrier transmissions represent the more appropriate communication tech-  
18 niques that can benefit from the relationship between distance and bandwidth in  
19 the range (4–10) THz.

## References

- [1] I. F. Akyildiz, J. M. Jornet, The Internet of Nano-Things, *IEEE Wireless Communication Magazine* 17 (6) (2010) 58–63.
- [2] J. Jornet, I. Akyildiz, Channel modeling and capacity analysis for electromagnetic wireless nanonetworks in the terahertz band, *Wireless*

- Communications, *IEEE Transactions on* 10 (10) (2011) 3211–3221. doi:10.1109/TWC.2011.081011.100545.
- [3] I. Llatser, A. Mestres, S. Abadal, E. Alarcon, H. Lee, A. Cabellos-Aparicio, Time- and frequency-domain analysis of molecular absorption in short-range terahertz communications, *Antennas and Wireless Propagation Letters*, *IEEE* 14 (2015) 350–353. doi:10.1109/LAWP.2014.2362194.
- [4] G. Piro, K. Yang, G. Boggia, N. Chopra, L. Grieco, A. Alomainy, Terahertz communications in human tissues at the nanoscale for healthcare applications, *Nanotechnology*, *IEEE Transactions on* 14 (3) (2015) 404–406. doi:10.1109/TNANO.2015.2415557.
- [5] C. Han, A. Bicen, I. Akyildiz, Multi-ray channel modeling and wideband characterization for wireless communications in the terahertz band, *Wireless Communications*, *IEEE Transactions on* 14 (5) (2015) 2402–2412. doi:10.1109/TWC.2014.2386335.
- [6] C. Zhang, C. Han, I. F. Akyildiz, Three dimensional end-to-end modeling and directivity analysis for graphene-based antennas in the terahertz band, in: *2015 IEEE Global Communications Conference (GLOBECOM)*, 2015, pp. 1–6. doi:10.1109/GLOCOM.2015.7417131.
- [7] C. Han, A. Bicen, I. Akyildiz, Multi-wideband waveform design for distance adaptive wireless communications in the terahertz band, *Signal Processing*, *IEEE Transactions on* 64 (4) (2016) 910–922.
- [8] A. Lakhtakia, R. Messier, *Sculptured thin films: nanoengineered morphology and optics*, SPIE Press monograph, 2015.



- [9] F. Fang, Y. Cheng, Dual-band terahertz chiral metamaterial with giant optical activity and negative refractive index based on cross-wire structure, *Progress In Electromagnetics Research M* 31 (2013) 59–69.
- [10] B. Wang, T. Koschny, M. Kafesaki, C. M. Soukoulis, Chiral metamaterials: Simulations and experiments, *J. Opt. A: Pure Appl. Opt.* 11.
- [11] N. Engheta, Chiral Materials and Chiral Electrodynamics: Background & Basic Physical Principles, in: *Special Workshop on Chiral and Complex Materials Progress in Electromagnetics Research Symposium*, 1991.
- [12] A. Lakhtakia, Recent contributions to classical electromagnetic theory of chiral media: what next?, *Speculations in Science and Technology* 14 (1) (1991) 2–17.
- [13] I. Lindell, A. Sihvola, S. Tretyakov, A. Viitanen, *Electromagnetic waves in chiral and bi-isotropic media*, Artech House, 1994.
- [14] J. Zhou, D. R. Chowdhury, R. Zhao, A. Azad, H.-T. Chen, C. M. Soukoulis, A. J. Taylor, Terahertz chiral metamaterials with giant and dynamically tunable optical activity, *Phys. Rev. B* 86. doi:10.1103/PhysRevB.86.035448.  
URL <http://link.aps.org/doi/10.1103/PhysRevB.86.035448>
- [15] R. Zhao, T. Koschny, C. M. Soukoulis, Chiral metamaterials: retrieval of the effective parameters with and without substrate, *Optics express* 18 (4).
- [16] A. M. Vegni, V. Loscrí, Performance of a Chirality-affected Channel exhibiting Giant Optical Activity for Terahertz Communications, in: *accepted to ACM NanoCom 2016*, 2016, pp. 1–6.